ARTICLE

# Reactivity of Nanostructured $MnO_2$ in Alkaline Medium Studied with a Micro-Cavity Electrode: Effect of Synthesizing Temperature

**L. Benhaddad,[†] L. Makhloufi,*[,†] B. Messaoudi,[†] K. Rahmouni,[‡] and H. Takenouti[‡]**

Laboratoire de Technologie des Matériaux et Génie des Procédés (LTMGP), Département de Génie des Procédés, Université A. Mira, Route de Targa Ouzemmour, 06000 Béjaia, Algeria, and UPR 15 du CNRS, Laboratoire Interfaces et Systèmes Electrochimiques (LISE), UPMC, University Paris 06, Case 133, 4 place Jussieu, 75252 Paris Cedex 05, France

**ABSTRACT** The influence of synthesizing temperature of manganese dioxide ($MnO_2$) powders on their electrochemical reactivity in 1 M KOH was investigated. These powders were prepared chemically by the hydrothermal method by oxidation of $Mn^{2+}$ by ammonium peroxodisulphate. The observations by scanning electronic microscopy, energy-dispersive X-ray analyses, and transmission electron microscopy techniques on $MnO_2$ obtained at different temperatures show the formation of many nanometre scale sticks lumped together to form a spherical particle of several micrometers. The results obtained by BET and BJH methods reveal mesoporous texture, and the $MnO_2$ synthesized at 90 °C presents the largest expanded surface area. The electrochemical reactivity of these powders in 1 M KOH was characterized with microcavity electrode by cyclic voltammetry and electrochemical impedance spectroscopy. The results illustrate that the nanostructured $MnO_2$ powder synthesized at 90 °C shows the highest electrochemical reactivity in agreement with BET data. The X-ray powder diffraction identified the $\gamma$-$MnO_2$, known as the most reactive species.

**KEYWORDS:** hydrothermal processing • cyclic voltammetry • EIS • BET surface area • cavity microelectrode

## 1. INTRODUCTION

Materials having structures of nanometer range (commonly named nanostructures) give rise to a considerable amount of current research because of their outstanding properties such as large expanded surface area and short distance for diffusion of molecules. As a consequence, they are expected to exhibit higher catalytic activity (1, 2) and faster ion exchange (3).

According to its electrochemical and thermodynamic properties, manganese and its oxides are good candidates as materials for positive or negative electrodes of primary and secondary batteries (4). Among these metal oxides, manganese dioxide has attracted much attention from chemists in recent times because it is stable in both aqueous and organic electrolytes and is reasonable in cost. The manganese oxides are known in many crystalline forms. $\alpha$-, $\beta$-, and $\gamma$-forms have tunnel structures with channels of various sizes, whereas $\delta$-$MnO_2$ has a layered structure and $\lambda$-$MnO_2$ that of a spinel (5).

Manganese dioxide can be used for many purposes: cathode for both aqueous and nonaqueous batteries, in corrosion protection of stainless steels (6), catalyst for chemical oxidation of various compounds in combination with other transition metal elements (7, 8), and electrocatalyst for oxygen reduction in alkaline solutions (9−11).

The reactivity of manganese dioxide generally depends on its structure and increases with hydration degree and with surface area (12). The $\gamma$-form, which generally exhibits the highest electrochemical reactivity, consists of an intergrowth structure of pyrolusite (1 × 1) and ramsdellite (1 × 2). It is widely used as cathodic material in batteries, especially that obtained by electrochemical oxidation of $Mn^{2+}$ referred as electrolytic manganese dioxide (EMD). Because of the large energy cost of the electrolysis method, great effort has been made to prepare an electrochemically active $\gamma$-$MnO_2$ by chemical methods with controlled morphologies, crystalline structures, and high surface area, including thermal, sol−gel, electrochemical, and hydrothermal methods (13−15). The physicochemical properties of $\gamma$-$MnO_2$ vary considerably with synthesis methods and experimental conditions. Defects have largely been considered as crucial factors to determine the electrochemical behaviour of $\gamma$-$MnO_2$ (16, 17). However, other properties such as pore size, pore types, particle size, morphology, and surface area, which also contribute to the electrochemical reactivity of $\gamma$-$MnO_2$ materials, have not been investigated in detail.

The objective of the present study was aimed at synthesizing manganese dioxide powders by the hydrothermal method at different temperatures and then comparing their morphologies, surface areas, and pore size distribution. Various electrolytes were used in the literature to study the electrochemical behaviour of $MnO_2$: acid medium (18) for Leclanché type battery application, neutral medium (19−21) particularly for super-capacitor, and alkaline medium (22−24)

* Corresponding author. E-mail: laid_mak@yahoo.fr. Tel/fax: 213 34 21 51 05.
Received for review October 14, 2008 and accepted January 2, 2009
[†] Université A. Mira.
[‡] University Paris 06.
DOI: 10.1021/am800118y



Published on Web 02/04/2009

for battery use. Though no stabilizing element was added in $MnO_2$ in the present study, we examined a relation between the structure and the electrochemical reactivity of these powders in 1 M KOH.

The electrochemical reactivity of these powders in the test medium was investigated by microcavity electrode and their structures and morphologies were characterized by scanning electron microscopy (SEM), transmission electron microscopy (TEM), energy-dispersive X-ray elemental analysis (EDX), and X-ray diffraction (XRD) techniques. Brunauer–Emmett–Teller (BET) and Barrett–Joyner–Halenda (BJH) methods were used, respectively, to evaluate the surface areas and the pore size distribution of powders.

The influence of synthesizing duration on the structure and electrochemical reactivity of $MnO_2$ powders synthesized by hydrothermal method was presented in a previous paper (25). It was shown that 24 h of synthesis are necessary to obtain a large expanded surface area and a highly reactive $MnO_2$. This is the synthesizing duration adopted in the present work.

## 2. EXPERIMENTAL SECTION

**2.1. Synthesis of $MnO_2$.** Experimental conditions for $MnO_2$ synthesis by hydrothermal method and those of its characterisations will be presented successively.

Manganese sulphate ($MnSO_4{\cdot}H_2O$) and ammonium peroxodisulphate ($(NH_4)_2S_2O_8$) were purchased from Prolabo products and were used as received. All the solutions were prepared with deionized water with double ion exchange columns.

Manganese dioxide ($MnO_2$) is chemically synthesized by hydrothermal method, which consists of mixing 0.08 mol of $MnSO_4 \cdot H_2O$, 0.08 mol of $(NH_4)_2S_2O_8$, and 150 mL of deionized water at room temperature. The mixture was stirred for 10 min to form a homogeneous pink solution, and then the synthesis itself was carried out for 24 h at different temperatures (60, 90, and 120 °C). As a result, black powders were obtained, which were filtered, rinsed with deionized water several times, and finally dried at 60 °C for 24 h.

The chemical synthesis of $MnO_2$ powders occurs according to the following reaction

$$MnSO_4 + (NH_4)_2S_2O_8 + 2H_2O \rightarrow MnO_2 + (NH_4)_2SO_4 + 2H_2SO_4 \quad (1)$$

The electrochemical reactivity of synthesized manganese dioxide powders was investigated in an alkaline solution of 1 M KOH. This solution was prepared with KOH (Merck product) and deionized water.

**2.2. Experimental Devices.** The electrochemical experiments were carried out in a usual cell containing three electrodes: microcavity electrode as working electrode, calomel reference electrode in saturated KCl solution (SCE), and platinum grid of large surface area as counter electrode. The cavity microelectrode consisted in a platinum microelectrode (60 $\mu$m in diameter) sealed in a large glass tube (8 mm in diameter) (26). A small cylindrical cavity (50 $\mu$m in diameter and 25 $\mu$m in depth) was obtained by a laser ablation of the platinum wire. This cavity was filled with the $MnO_2$ powder using the electrode as a pestle. This method constituted a marked advantage to study the $MnO_2$ powder itself. First, the electrochemical process taking place at the substrate/electrolyte interface was discarded; second, a thin powder layer allowed the minimization of the in-depth distribution of both potential and current, and finally, only a small amount of $MnO_2$ is needed. The volume of the cavity used is $50 \times 10^{-9}$ cm$^3$ (26). With the apparent specific gravity of $MnO_2$ powder estimated to 2.2, the mass necessary will be 110 ng to perform experiments. The grinding of $MnO_2$ into a fine powder before its introduction into the cavity permitted likely to homogenize $MnO_2$ powder to be analysed. Consequently, this method also allowed the achievement of well-reproducible results.

Electrochemical measurements including cyclic voltammetry (CV) and electrochemical impedance spectroscopy (EIS) were carried out with a Potentiostat allowing measurements of low current and huge impedance (Gamry, Femstat FAS1). Both, the potentiostat and the electrochemical cell were set into a Faraday cage. The electrochemical impedance spectroscopy (EIS) measurements were carried out at the potential of open circuit just before the beginning of each experiment with ac amplitude of 10 $mV_{rms}$ in the frequency range from 10 kHz to 10 mHz or 1 mHz with a density of 10 points per decade. The impedance data were analyzed with in-house made software based on a Simplex parameter regression.

**2.3. Characterisation of $MnO_2$.** A SEM (Leica Stereoscan 440) at 20 keV acceleration allowed the observation of the morphology of manganese dioxide powders. The kind of imaging used is secondary electron. The SEM device was coupled with EDX (Princeton Gamma-Tech) to determine their elemental compositions. In addition to these techniques, the X-ray powder diffraction (XRD) and TEM techniques were also used. TEM images were obtained with a JEOL 2000 FX microscope running at an accelerating voltage of 200 keV. Prior to analysis, the $MnO_2$ powder was crushed in a mortar. A small amount was then added in a small volume of pure ethanol using ultrasonic bath. A drop of this mixture was placed on a copper grid covered with a carbon coating and it was allowed to dry in air.

**2.4. Determination of the Surface Area and the Pore Size Distribution.** Isotherms of $N_2$ adsorption/desorption, pore size distributions, and BET surface areas were determined on a micromeritics instrument. Prior to analysis, $MnO_2$ samples were first purged under a vacuum at 80 °C to remove surface water, which would interfere with the instrument. $N_2$ adsorption and desorption isotherms were then collected at 77 K. The pore size distributions in the mesopore and micropore regions and the surface areas of samples were measured using the Barrett–Joyner–Halenda (BJH) and the Brunauer–Emmett–Teller (BET) models, respectively.

## 3. RESULTS AND DISCUSSION

The morphology and the structure of synthesized $MnO_2$ powders at different temperatures will be presented first. The results relative to the electrochemical reactivity of $MnO_2$ in 1 M KOH solution will then be described.

**3.1. Morphological and Structural Characterizations.** The morphology of synthesized $MnO_2$ powders observed by SEM technique, shown in Figure 1, indicate that all the products consisted of many fine sticks heaped together to form bowls of several $\mu$m in diameter. It is also apparent that there is very little difference in morphology between these three samples, indicating that the synthesizing temperature has little effect on morphology in this size range. Elemental analysis by EDX (Figure 1) confirms the presence of manganese and oxygen, elemental components of $MnO_2$. The presence of sulphur, as an impurity, was more marked in the case of $MnO_2$ powder synthesized at 120 °C.

Typical TEM images (Figure 2) show that the tiny sticks observed by SEM on $MnO_2$ powders consisted of assembling straight needles with diameters in the range of 20–50 nm and lengths up to several hundred nanometers. These im-

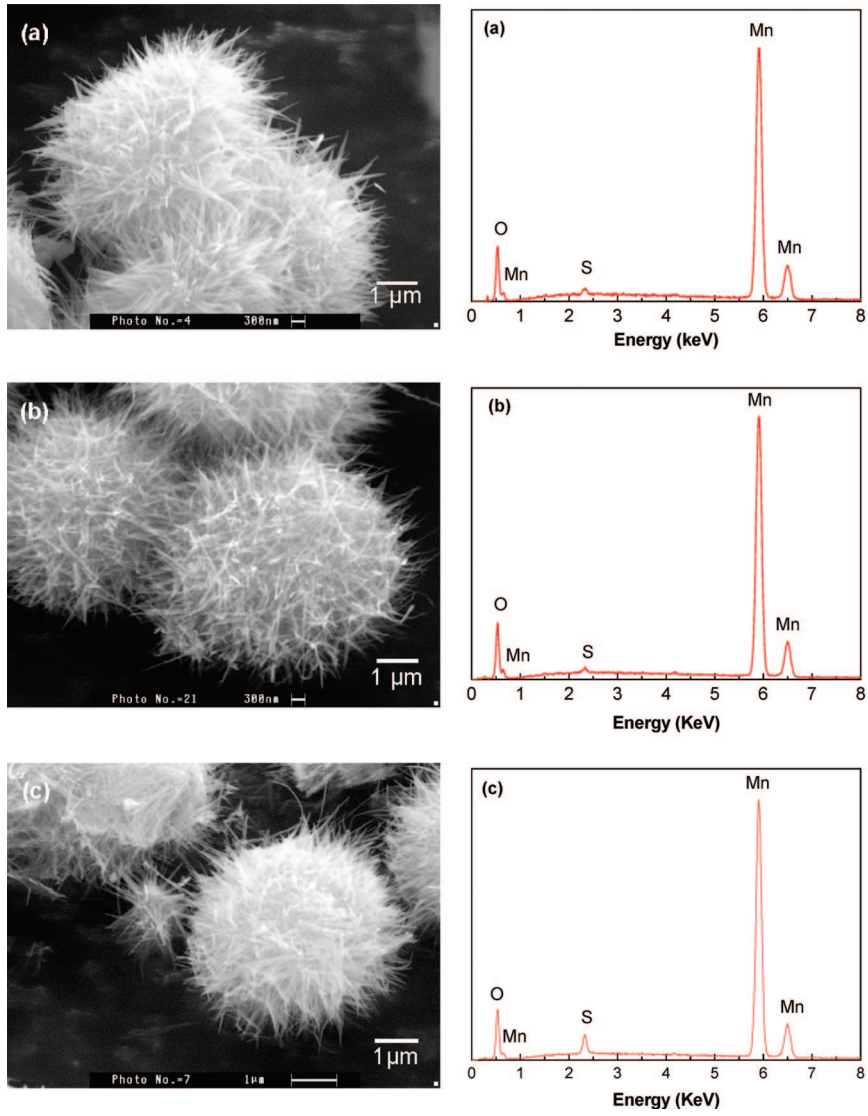


**FIGURE 1. SEM pictures and corresponding EDX profiles of $MnO_2$ powders synthesized at different temperatures: (a) 60, (b) 90, and (c) 120 °C.**

ages allow us to call the synthesized $MnO_2$ powders as nanostructured materials. Electron diffraction pattern showed that each stick is rather well-crystallized but its orientation changes from one stick to another. The needle is thus polycrystalline structure.

The nitrogen adsorption/desorption isotherms (Figure 3) show a substantial hysteresis loop in the $P/P_0$ range above 0.6, which is due to the evaporation of $N_2$ gas slower than that expected from the free surface as a result of surface tension phenomena associated with the liquefied adsorbate (27). Consequently, this feature indicates the presence of mesopores in the structure of $MnO_2$ powders.

At relative pressures $P/P_0$ greater than 0.8, a rapid increase in the volume of adsorbed gas was observed that was due to the condensation of the adsorbate in the larger pores formed between particles because of the particle size distributions (27, 28). The surface area of each product was determined by BET isotherm in conjunction with $N_2$ adsorption data collected over the relative pressure range from 0.06 to 0.2 at 77 K. In fact, at low relative pressures, the isotherm underpredicts actual adsorption because of the adsorption energies higher than expected value because of the surface inhomogeneity. In contrast, at relatively high relative pressures, the BET isotherm overestimates adsorption because of limitations associated with liquefaction of the adsorbate (27, 28).

The BET isotherm is expressed as follows

$$\frac{P}{V_a(P_0 - P)} = \frac{1}{V_m C} + \frac{C-1}{V_m C}\frac{P}{P_0} \qquad (2)$$

Where $V_a$ is the volume of gas adsorbed at $P/P_0$ ($cm^3\ g^{-1}$); $V_m$ is the volume of gas that would occupy a monolayer ($cm^3\ g^{-1}$); $C$ is a constant for the gas/solid pair; $P$ and $P_0$ are the equilibrium and the saturation pressures of adsorbate at the temperature of adsorption, respectively. The plot of $P/\{V_a(P_0 - P)\}$ versus $P/P_0$ give a straight line whose intercept is $1/V_mC$ and whose slope is $(C - 1)/V_mC$. Thus from the slope and intercept, the two constants $V_m$ and $C$ can be evaluated, and consequently, the expanded surface area is calculated from the following expression

$$S = 4.35V_m \qquad (3)$$

The obtained values of BET surface area of $MnO_2$ powders synthesized at different temperatures determined with ex-

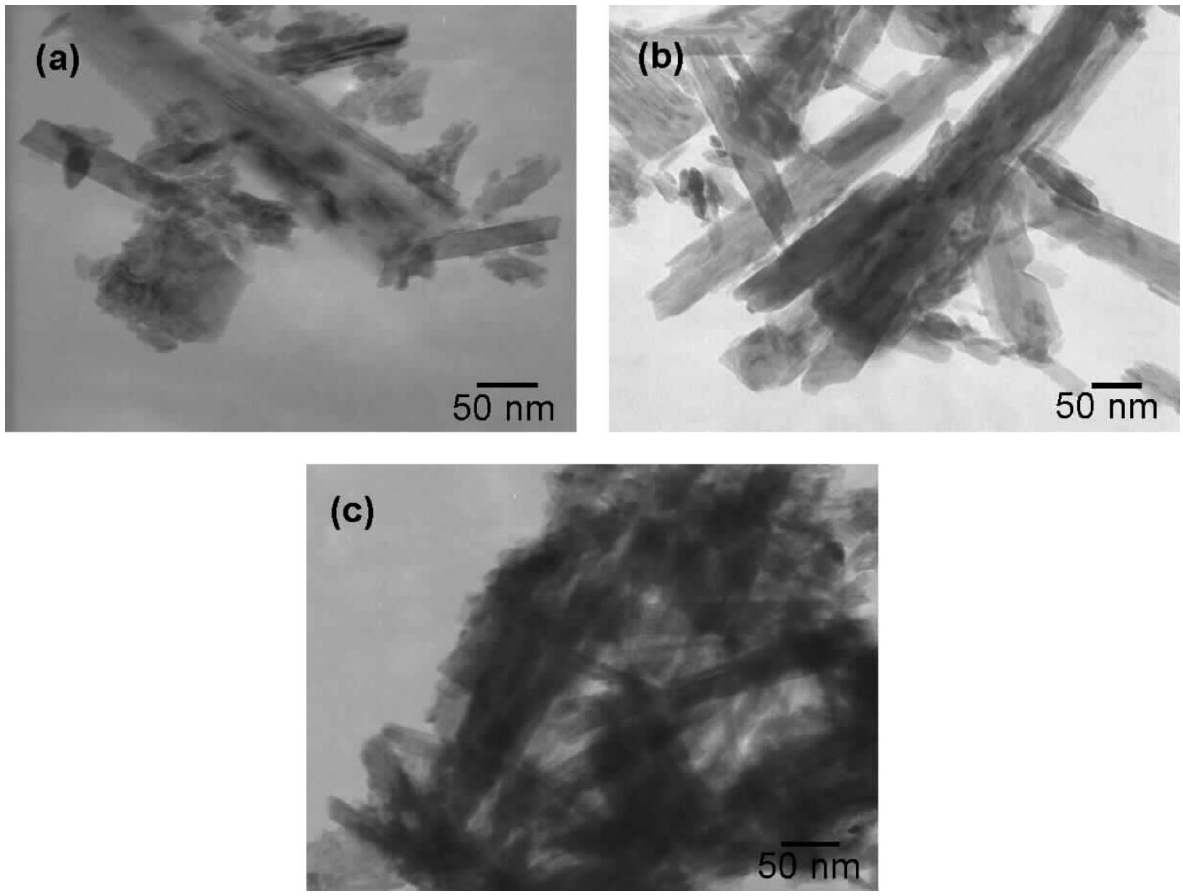


**FIGURE 2. TEM images of $MnO_2$ powders synthesized at different temperatures: (a) 60, (b) 90, and (c) 120 °C.**

pression (3) are displayed in Table 1 together with BJH data. These values show that the $MnO_2$ powders are porous materials and the texture of these pores are changing when the synthesizing temperature is varied. It is noteworthy that the total surface area of a porous electrode is the sum of the surface area contributed from all the pores (29). The $MnO_2$ synthesized at 90°C shows the largest surface area and the largest pore volume. The maximum expanded surface area reached 90.8 $m^2\ g^{-1}$.

The surface area of a given mass of solid powder material is closely related to the size of the constituent particles. Those powder particles stick together and pores are formed in those aggregated particles. Pore size and pore size distribution depend on the size and shape of the powder particles and how they are packed together (29). The pore size distribution for the three $MnO_2$ powders determined by BJH method is shown in Figure 4. It appears that all these powders consist of a large distribution of mesopores with pore radii between 5 and 50 nm. Two peaks were detected in the pore distribution, which explains the presence of two porosities: a larger one, ca. 80 nm corresponding to the pores between sticks observed inside the $MnO_2$ bowls (Figure 1), and another around 10−20 nm are formed between the nanoneedles making the sticks (Figure 2).

According to these results, it can be noted that the synthesizing temperature has a great effect on the pore-size distribution of the synthesized $MnO_2$ powders. It was concluded that the increase of temperature from 60 to 90 °C leads to a slight enlargement of pores size and pores volume, consequently an increase in its surface area. However, a decrease in the surface area of $MnO_2$ synthesized at 120 °C was observed, which may be explained by intercrystallite rearrangements leading to the progressive sintering of pores under the temperature effect, which decreases its pores size and pores volume.

X-ray diffraction is the most common tool used to characterize the crystal structure of manganese dioxide. X-ray diffraction pattern of $MnO_2$ powder synthesized at 90 °C exhibiting the largest BET surface area is shown in Figure 5. The peaks observed were assigned by atomic distance (Å) and (*hkl*) values: 3.98 (120), 2.40 (131), 2.13 (300), 1.42 (421), and 1.63 (160). All of the reflections of the XRD pattern can be readily indexed to the crystallographic variety gamma ($\gamma$-$MnO_2$) with the lattice constants $a = 1.020$ nm and $c = 0.798$ nm, which agree with the values reported in the literature (JCPDS Card no. 14-0644). The peaks assigned by atomic distance (Å) and (*hkl*) of 2.57 (301), 1.53 (312), and 1.82 (302) can be indexed to the crystallographic variety ramsdellite ($\beta$-$MnO_2$) and that assigned to 3.11 (110) is indexed to the pyrolusite ($\beta$-$MnO_2$), which means that this powder consists of $\gamma$-$MnO_2$ formed in the matrix of ramsdellite with the presence of pyrolusite. It was reported in the literature that the $\gamma$-$MnO_2$ structure is considered as a ramsdellite matrix with randomly distributed intergrown microdomains of pyrolusite (17, 30).

The X-ray diffraction patterns of $MnO_2$ powders synthesized at 60 and 120°C are presented in patterns a and b in

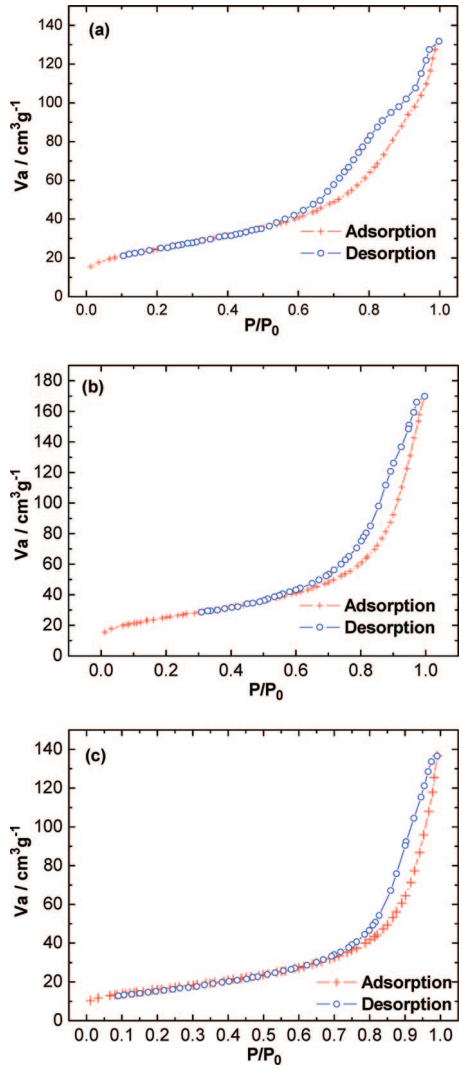


FIGURE 3. $N_2$ adsorption/desorption isotherms for $MnO_2$ powders synthesized at different temperatures: (a) 60, (b) 90, and (c) 120 °C.

**Table 1. Properties of the $MnO_2$ Powders Synthesized by the Hydrothermal Method at Different Temperatures**

| | *T* (°C) | | |
|---|---|---|---|
| | 60 | 90 | 120 |
| BET surface area ($m^2$ $g^{-1}$) | 88.5 | 90.8 | 56.4 |
| average pore size (nm) | 8.30 | 10.5 | 12.9 |
| total pore volume ($cm^3$ $g^{-1}$) | 0.184 | 0.24 | 0.182 |

Figure 6, respectively. The pattern relative to $MnO_2$ synthesized at 60°C reveal that its crystallographic variety is, in major part, akhtenskite ($\varepsilon$-$MnO_2$) which has a hexagonal unit cell with the lattice constants $a = 28$ nm and c = 44.5 nm, and the presence of pyrolusite assigned by atomic distance (Å) and (*hkl*) of 1.40 (110), which has a tetragonal unit cell with $a = 0.439$ nm and c = 0.287 nm. The peaks observed in the pattern relative to $MnO_2$ synthesized at 120 °C reveal the crystallographic variety of ramsdellite ($\beta$-$MnO_2$), which is less reactive than these two varieties and has an orthorhombic unit cell with $a = 0.446$ nm and $c = 0.285$ nm.

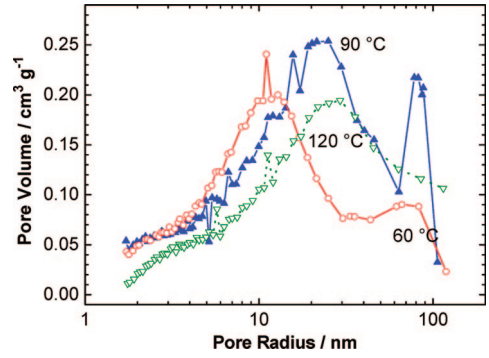


FIGURE 4. Comparison of pores size distribution of $MnO_2$ powders synthesized at different temperatures (calculated by BJH method).

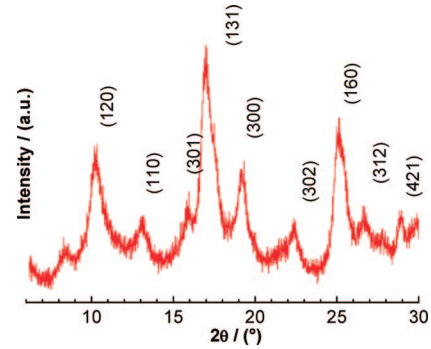


FIGURE 5. XRD pattern of $MnO_2$ synthesized at 90 °C.

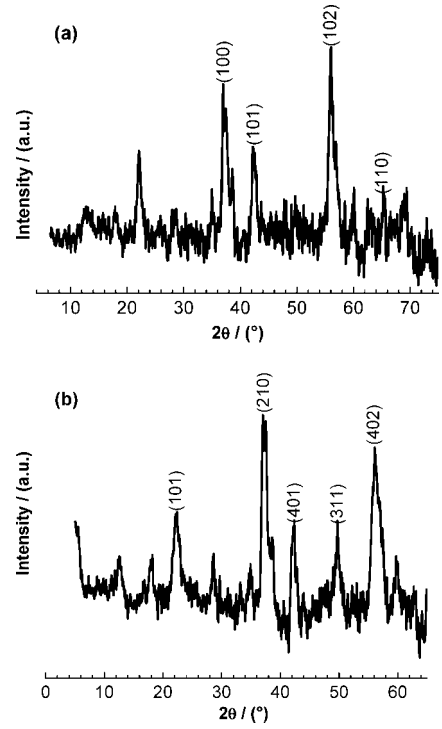


FIGURE 6. XRD patterns of $MnO_2$ synthesized at (a) 60 and (b) 120 °C.

As mentioned above, the defects have been studied intensively because they affect the electrochemical behaviour of manganese dioxide. According to Chabre and Pannetier (17), two types of defects are present. One is De Wolff disorder, which is formed from the insertion of pyrolusite structural units into a ramsdellite matrix, relating to the amount of pyrolusite units. The other type is called microt-

**Table 2. Line Shifts Due to Microtwinning and De Wolff Disorder**

| | | $2\theta$ shift[a] | |
|---|---|---|---|
| *hkl* | $2\theta$ (Cu Kα) | microtwinning | De Wolff disorder |
| 110 | 21.8 | − | + |
| 130 | 35.1 | + | − |
| 021 | 36.8 | − | * |
| 111 | 38.4 | − | − |
| 040 | 38.8 | − | * |
| 200 | 39.7 | * | * |
| 121 | 42.0 | + | * |
| 140 | 43.8 | − | * |
| 131 | 47.7 | − | + |
| 221 | 55.3 | + | * |
| 240 | 56.8 | − | * |
| 231 | 60.0 | − | + |
| 151 | 63.1 | + | − |
| 002 | 65.0 | + | * |
| 061 | 69.0 | − | * |
| 330 | 69.2 | + | − |
| 112 | 69.5 | − | + |
| 301 | 70.4 | − | * |
| 311 | 71.2 | − | − |

[a] +, High angle; −, low angle; *, no shift.

winning defects, which are generated by twinning of (021) and (061) planes within the ramsdellite blocks. The two types of defects modify the shape, position, and relative intensity of some diffraction lines. The line ($2\theta$) shifts are summarized in Table 2.

It was observed that $MnO_2$ synthesized at 60°C exhibited high fraction of De Wolff disorder, characterized from the shift of (110) planes to higher angle ($2\theta$, 66.7°), demonstrating the presence of pyrolusite units in the structure of akhtenskite ($\varepsilon$-$MnO_2$). However, by increasing synthesizing temperature to 90°C, the manganese dioxide showed low fraction of De Wolff disorder characterizing from the shift of (110) planes to lower angle ($2\theta$, 13°), which means that the amount of pyrolusite decreases by increasing synthesizing temperature because of the intergrowth of pyrolusite and ramsdellite to give rise to $\gamma$-$MnO_2$.

From XRD and BET surface area results, it can be concluded that the synthesizing temperature affects the crystal structure of obtained manganese dioxide powders. Indeed, the increase of synthesizing temperature from 60 to 90°C engenders the transformation of $\varepsilon$-$MnO_2$ to $\gamma$-$MnO_2$ and the diminution of defects, leading to a very slight increase in BET surface area (88.5 to 90.8 $m^2\ g^{-1}$) and a decrease in unit-cell parameters. On the other hand, the decrease in BET surface area at temperature superior to 90°C is explained by the transformation of $\gamma$-$MnO_2$ to $\beta$-$MnO_2$ (ramsdellite) and the decrease in unit cell parameters.

The influence of temperature on the crystal structure of manganese dioxide is studied in the case of EMD by J.B. Arnott et al. (28), who found that a structural and micropore analysis of a series of heat treated electrolytic manganese dioxide samples shows that the original EMD with $\gamma$-$MnO_2$ structure

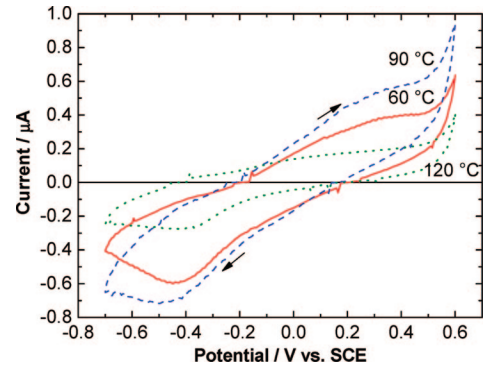


**FIGURE 7. Polarization curves in 1 M KOH of $MnO_2$ powders synthesized at different temperatures, potential scan rate at 0.2 V $s^{-1}$.**

was found to progressively convert to $\beta$-$MnO_2$ at elevated temperatures leading to a greater degree of transformation.

**3.2. Electrochemical Reactivity of $MnO_2$.** The electrochemical reactivity of $MnO_2$ powders obtained at different synthesizing temperatures was studied by both cyclic voltammetry and electrochemical impedance spectroscopy.

***3.2.1. Cyclic Voltammetry.*** First, the reactivity of $MnO_2$ powders was evaluated by the cyclic voltammetry (CV). Each powder was pounded and 100−150 ng of powders were pressed into the cavity of the microelectrode. Then, the electrode was transferred into 1 M KOH solution at 25 °C without purging dissolved oxygen. Then, after 1 min of stabilization time at the open circuit potential, the cyclic voltammetry measurements were carried out. The potential scan rate was 0,2 V $s^{-1}$ and started from the open-circuit potential towards the negative direction up to −0.7 V vs SCE, followed by the anodic scan up to 0.6 V vs. SCE. The voltammograms obtained at the first scan are shown in Figure 7.

During the cathodic scan and in all these voltammograms, a current peak can be observed at a potential of ca. −0.4 V vs. SCE. According to Toupin et al. (31), two mechanisms can explain this phenomenon. The first one implies the intercalation of protons ($H^+$) or alkali metal cations ($K^+$) in the bulk of the material upon reduction followed by deintercalation upon oxidation:

$$MnO_2 + H^+ + e^- \rightarrow MnOOH \quad (4)$$

Or

$$MnO_2 + K^+ + e^- \rightarrow MnOOK \quad (5)$$

The second mechanism is based on the surface adsorption of electrolyte cations ($K^+$) on $MnO_2$

$$(MnO_2)_{surface} + K^+ + e^- \rightarrow (MnO_2^- K^+)surface \quad (6)$$

It should be noticed that both proposed mechanisms involved a redox reaction between the III and IV oxidation states of Mn.

Kozawa et al. (32, 33) described a two-step mechanism. In the first step (electron−proton mechanism), an electron from the external circuit is inserted into the manganese dioxide structure to reduce a $Mn^{4+}$ ion to $Mn^{3+}$. To maintain structural charge balance, a water

molecule present at the manganese dioxide|electrolyte interface dissociates into a proton, which is inserted into the structure, and an $OH^-$ ion that remains in the electrolyte. The presence of protons was identified by neutronic spectroscopy by C. Cachet et al. (34). Given that protons transport is widely believed to be the rate limiting property in the discharge of manganese dioxide (35), the facility with which protons are inserted into the structure is a key electrochemical property. It is reported in the literature that $MnO_2$ has a reduction potential very close to that of oxygen in alkaline solution, and may undergo electroreduction earlier or along with oxygen reduction because of the sluggish kinetics of oxygen reduction. The mechanism of the oxygen reduction was proposed to be a coupled reaction, involving the redox pair $MnO_2$/MnOOH (11). It is generally accepted that electro-catalytic activity of $MnO_2$ for oxygen reduction is resulted from the catalytic decomposition of hydrogen peroxide ions generated as an intermediate species during oxygen reduction (36). It is well known that because the catalytic process for oxygen reduction involves the reduction and oxidation of surface manganese ions, the number and activity of these redox sites would be important factors for a better catalytic activity.

During the anodic scan, a broad current peak was observed in the three voltammograms at a potential close to 0.3 V vs. SCE. This peak corresponds to the oxidation of MnOOH (or MnOOK), formed previously by cathodic sweep, to $MnO_2$ according to the reverse reactions of (4) and (5). The comparison of these three voltammograms shows that the $MnO_2$ synthesized at 120 °C, having the lowest BET surface area, exhibits the lowest cathodic and anodic peak intensities; $MnO_2$ synthesized at 90 °C exhibits the largest BET surface area and shows the highest cathodic and anodic peak intensities. The high values of these intensities reveal the highest electrochemical reactivity of this powder in 1 M KOH medium. Because we used a microcavity electrode, and thus the exact amount of $MnO_2$ inserted in it is unknown. As stated above, however, this amount was between 100 and 150 ng. To give just the idea about the order of magnitude, let us consider that this amount being roughly 110 ng; the charge involved during the reduction reaction then allowed the evaluation of the specific charge as ca. 162.5, 234.6, and 69.3 $\mu$C $g^{-1}$, respectively, for $MnO_2$ synthesized at 60, 90, and 120 °C.

### *3.2.2. Electrochemical Impedance Spectroscopy.*

The impedance technique (EIS) has been used to characterize the $MnO_2$ powders synthesized at different temperatures in order to compare their electrochemical reactivities. Impedance spectra presented in Nyquist plot were obtained in 1 M KOH in the frequency range from 10 KHz to 1 mHz (Figure 8).

The Nyquist diagrams of EIS data exhibit, though badly separated, two capacitive loops in the high- and medium-frequency range and a linear branch in the low frequencies.

These impedance spectra may be represented by an electrical equivalent circuit presented in Figure 9.

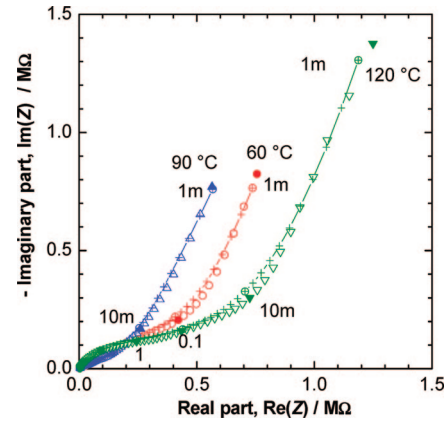


**FIGURE 8. Nyquist plots of impedance spectra obtained in 1 M KOH with $MnO_2$ powders synthesized at different temperatures. Symbols: triangle and circles, experimental; +, regressed data with the circuit illustrated in Figure 9.**

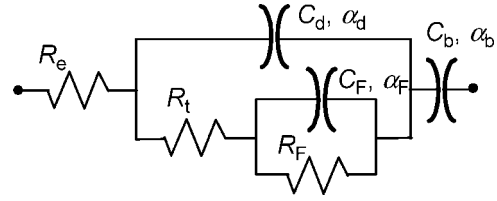


**FIGURE 9. Equivalent electrical circuit to represent the EIS data.**

In this circuit:

$R_e$ represents the electrolyte resistance between the reference and the working electrode; $R_t$ and $C_d$ are allocated, respectively, to the charge transfer resistance in parallel with the double layer capacitance; $R_F$ and $C_F$ stand for faradaic impedance associated with the reduction of dissolved oxygen as it is allocated to cyclic voltammetry curves; $C_b$ characterizes the capacitance associated with charge storage in the chemical form, i.e., corresponding to cation intercalation/deintercalation process. Therefore, this capacitance is an important parameter in the use of $MnO_2$ as battery material; $\alpha_d$, $\alpha_F$, and $\alpha_b$ are depression coefficients with values between 0 and 1.

To compare the electrochemical reactivity of these powders in 1 M KOH medium, it is appropriate to evaluate the values of $C_b$. For this purpose, a simplex parameter regression calculation was applied. It was considered that the $R_t$–$C_d$ couple exhibit the highest-frequency domain (centered at about 100 Hz) and the $R_F$–$C_F$ couple exhibit the medium-frequency domain (1 Hz domain). The $C_b$ expresses itself at the lowest-frequency domain.

The obtained results reveal that the charge storage capacitances of the $MnO_2$ powders synthesized at 60, 90, and 120°C are equal to 3.9, 7.1, and 2.4 $\mu$F, respectively. These values show that the $MnO_2$ powder synthesized at 90 °C has the highest value of $C_b$, which confirms the insertion of the largest quantity of charges in the chemical form in its structure, which is attributed in major part to its high surface area. This result is in good agreement with that obtained with cyclic voltammetry. Indeed, the powder having the largest BET surface area presents the highest electrochemical reactivity in 1 M KOH. Provided that the amount of $MnO_2$ filled into the micro-cavity

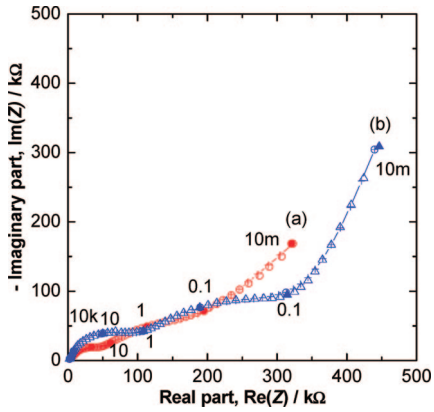


**FIGURE 10. Nyquist plots in 1 M KOH of $MnO_2$ powder synthesized at 90°C: (a) as-synthesized, (b) aged by 10 potential scans at 0.01 V $s^{-1}$. Symbols: circles and triangles, experimental; +, regressed data with the circuit illustrated in Figure 9.**

electrode being 110 ng, the specific capacitance is evaluated to be equal to 65 F $g^{-1}$, the values often reported for a very high performance EMD.

To evaluate the effect of charge–discharge cycling on the battery performance, the $MnO_2$ synthesized at 90 °C is submitted to cyclic voltammetry for 10 scans at 0.01 V $s^{-1}$ in 1 M KOH solution, and the EIS measurements were carried out in the frequency range from 10 KHz to 10 mHz. The obtained spectrum was presented in Figure 10. For comparison, the EIS spectrum of $MnO_2$ before potential cycling is overlaid on this figure.

The impedance spectra exhibited the same features, two capacitive loops and a capacitive branch at the low frequency end. The comparison of these two spectra reveals an enlargement of the Nyquist diagram indicating an increase in charge transfer and faradaic resistances with potential cycling. This phenomenon can be probably attributed to the decrease in the active sites of $MnO_2$ powder because of their saturation by ionic and proton diffusions, or to mechanical failure of the powder during cycling. This makes the diffusion of protons into the structure of $MnO_2$ too difficult, which engenders a progressive decrease of the electrochemical reactivity of the $MnO_2$ powder in 1 M KOH by cycling.

The values of $C_b$ for the two spectra were found equal to 7.1 and 16.5 $\mu$F, respectively, for $MnO_2$ as synthesized and aged by potential cycling. This confirms our previous results and a greater charge is inserted into aged $MnO_2$ in 1 M KOH, in spite of a progressive decrease of its reactivity as observed by cyclic voltammetry.

## 4. CONCLUSIONS

In summary, it has been shown that the synthesis of nanostructured $MnO_2$ powders was successfully realised by hydrothermal method at different synthesizing temperatures. The influence of temperature on the physical properties and electrochemical reactivity of these powders in 1 M KOH was investigated.

It can be concluded from experimental results presented above that the synthesizing temperature influences both the physical properties like surface area, pore size, pore size distribution, and the electrochemical reactivity of these powders. Indeed, the comparison of the electrochemical reactivity of these powders in 1 M KOH shows that the $MnO_2$ synthesized at 90 °C, having the largest BET surface area, presents the highest electrochemical reactivity in this medium. Therefore, a marked reactivity of this powder is attributed to its large surface area and to its crystallographic variety. The XRD pattern reveals that synthesized $MnO_2$ is of $\gamma$-form, recognized as the most electrochemical reactive form. Also, the reactivity of these powders in 1 M KOH follows this order: $\gamma$-$MnO_2$ > $\varepsilon$-$MnO_2$ > $\beta$-$MnO_2$.

**Acknowledgment.** The present work was carried out in the frame of French–Algerian cooperation project CMEP-PHC Tassili No. 06 MDU 686. The authors are grateful for the efficient assistance of Mrs. Pilier and Mr. Borensztajn for TEM and SEM experiments and greatly appreciate Dr. Maurin for the XRD measurements and Dr. Lacroix, European Institute of Membrane at Montpellier, for his kind help with BET-BJH experiments.

## REFERENCES AND NOTES

(1) Van der Pol, A. J. H. P.; Van Hoof, J. C. H. *Appl. Catal. A* **1992**, *92*, 93.
(2) Castagnola, N.; Dutta, P. *J. Phys. Chem.* **1998**, *102*, 1696.
(3) Giraldo, O.; Marquez, M.; Brock, S. L.; Suib, S. L.; Hillhouse, H.; Tsapatsis, M. *J. Am. Chem. Soc.* **2000**, *122*, 12158.
(4) Messaoudi, B.; Joiret, S.; Keddam, M.; Takenouti, H. *Electrochim. Acta* **2001**, *46*, 2487.
(5) Sokol'skii, G. V.; Ivanov, S. V.; Ivanova, N. D.; Boldirev, E. I. *Powder Metall. Met. Ceram.* **2006**, *45* (3–4), 158.
(6) Olesen, B. H.; Avci, R.; Lewandowski, Z. *Corros. Sci.* **2000**, *42*, 211.
(7) Cadus, L. E.; Ferreti, O. *Appl. Catal., A* **2002**, *233*, 239.
(8) Gandia, L. M.; Vicente, M. A.; Gil, A. *Appl. Catal., B* **2002**, *38*, 295.
(9) Yang, J.; Xu, J. J. *Electrochem. Comm.* **2003**, *5*, 306.
(10) Lima, F. H. B.; Calegaro, M. L.; Ticianelli, E. A. *J. Electroanal. Chem.* **2006**, *590*, 152.
(11) Cao, Y. L.; Yang, H. X.; Ai, X. P.; Xiao, L. F. *J. Electroanal. Chem.* **2003**, *557*, 127.
(12) Rüetschi, P.; Giovanoli, R.; Buerki, P. *Proc. Manganese Dioxide Symp.* **1975**, *1*, 12.
(13) Muraoka, Y.; Chiba, H.; Atou, T.; Kikuchi, M.; Hiraga, K.; Syono, Y.; Sugiyama, S.; Yamamoto, S.; Grenier, J.-C. *J. Solid State Chem.* **1999**, *144*, 136.
(14) Ching, S.; Petrovay, D. J.; Jorgensen, M. L. *Inorg. Chem.* **1997**, *36*, 883.
(15) Reddy, R. N.; Reddy, R. G. *J. Power Sources* **2003**, *124*, 330.
(16) De Wolff, P. M. *Acta Crystallogr.* **1959**, *12*, 341.
(17) Chabre, Y.; Pannetier, J. *Prog. Solid State. Chem.* **1995**, *23*, 1.
(18) Jang, Y.; Huang, B.; Wang, H.; Sadoway, D.; Chiang, M. *J. Electrochem. Soc.* **1999**, *146*, 3217.
(19) Hansung, K.; Popov, B. N. *J. Electrochem. Soc.* **2003**, *150*, A1153.
(20) Hansung, K.; Popov, B. N. *J. Electrochem. Soc.* **2003**, *150*, A56.
(21) Brousse, T.; Toupin, M.; Bélanger, D *J. Electrochem. Soc.* **2004**, *151*, A614.
(22) Benhaddad, L.; Makhloufi, L.; Messaoudi, B.; Rahmouni, K.; Takenouti, H. *Matér. Tech.* **2007**, *95*, 405.
(23) Kloss, M.; Rahner, D.; Plieth, W. *J. Power Sources* **1997**, *69*, 137.
(24) Schlörb, H.; Bungs, M.; Plieth, W. *Electrochim. Acta.* **1997**, *42*, 2619.
(25) Benhaddad, L. ; Makhloufi, L.; Messaoudi, B.; Rahmouni, K.; Takenouti, H. *5th International Conference on Chemistry*; Cairo, Egypt, March 3–6, 2008; Department of Chemistry, University of Cairo: Cairo, Egypt, 2008.
(26) Vivier, V.; Cachet-Vivier, C.; Wu, B. L.; Cha, C. S.; Nedelec, J.-Y.; Yu, L. T. *Electrochem. Solid-State Lett.* **1999**, *2*, 385.

(27) Swinkels, D. A. J.; Bristow, N.; Williams, R. P. *Prog. Batt. Batt. Mater.* **1994**, *13*, 12.
(28) Arnott, J. B.; Williams, R. P.; Pandolfo, A. G.; Donne, S. W. *J. Power Sources* **2007**, *165*, 581.
(29) Qu, D. *Electrochim. Acta* **2003**, *48*, 1675.
(30) Turner, S.; Buseck, P. R. *Nature* **1983**, *304*, 143.
(31) Toupin, M.; Brousse, T.; Belanger, D. *Chem. Mater.* **2004**, *16*, 3184.
(32) Kozawa, A.; Yeager, J. F. *J. Electrochem. Soc.* **1965**, *112*, 959.
(33) Kozawa, A.; Yeager, J. F. *J. Electrochem. Soc.* **1968**, *115*, 1003.
(34) Cachet, C.; Belushkin, A.; Natkaniec, I.; Lecerf, A.; Fillaux, F.; Yu, L. T. *Physica B* **1995**, *213−214*, 827.
(35) Hong, Z.; Zhenhai, C.; Xi, X. *J. Electrochem. Soc.* **1989**, *136*, 2771.
(36) Rao, K. V.; Venkatesan, V. K.; Udupa, H. V. K. *J. Electrochem. Soc. India* **1982**, *31−32*, 33.

AM800118Y